Journal of Materials Chemistry A

PAPER

View Article Online
View Journal | View Issue

Cite this: *J. Mater. Chem. A*, 2018, **6**, 16515

Atomic layer deposited zinc oxysulfide anodes in Li-ion batteries: an efficient solution for electrochemical instability and low conductivity†

Soumyadeep Sinha,[a] Hari Vignesh Ramasamy,[b] Dip K. Nandi,[c] Pravin N. Didwal,[a] Jae Yu Cho,[a] Chan-Jin Park,[a] Yun-Sung Lee,[b] Soo-Hyun Kim[c] and Jaeyeong Heo*[a]

In addition to their optoelectronic applications, Zn-based oxides and sulfides have also been widely studied as electrode materials in Li-ion batteries owing to their high theoretical capacity. However, both the materials suffer from a drastic loss in capacity due to their poor conductivity and electrochemical instability. A very efficient and carefully controlled combination of these two may address these limitations. In this work, thin films of zinc oxysulfide (ZnOS) with an O/(O + S) ratio of ~0.7 were deposited using a combination of oxide and sulfide atomic layer deposition (ALD) cycles; they were then tested as anodes in Li-ion batteries. The material was grown directly on a stainless steel substrate (SS), characterized extensively using several *ex situ* characterization tools, and then used as an anode with no binder or conductive additives. Cyclic voltammetry measurements were used to confirm the reversible conversion of ZnOS in addition to the well-known alloying–dealloying Li–Zn reaction. The material loading was further optimized by varying the number of ALD supercycles to attain the maximum stable cycling performance. The highest stable capacities of 632.9 and 510.3 mA h g^{-1} were achieved at current densities of 0.1 and 1 A g^{-1} (~4 and 40 μA cm^{-2}), respectively, for a ZnOS film with an optimum thickness of ~75 nm. The optimized ZnOS anode exhibited superior electrochemical performance in comparison to the equivalent pristine ZnO and ZnS anodes. Finally, the post-cycling analysis of the binder-free ALD grown ZnOS anodes demonstrated excellent adhesion to the SS substrate and the high stability of these films upon cycling.

Received 4th May 2018
Accepted 27th July 2018

DOI: 10.1039/c8ta04129f

rsc.li/materials-a

1. Introduction

Secondary batteries (commonly known as rechargeable batteries) are necessary in modern society; Li-ion batteries (LIBs) are one of the most common types and are widely used in portable and high-power electronic devices. As these devices continue to decrease in size, more research is needed to design smaller batteries without losing capacity or other essential outputs. Several attempts have already been made in the fabrication and optimization of different active electrode materials. However, the increasing demand for high-power-supply (*e.g.*, electric vehicles) is no longer being fulfilled by current commercial LIBs owing to the low theoretical capacity (372 mA h g^{-1}) of conventional graphite anodes.[1–5] Therefore, it is essential to develop new anode materials with a significantly higher capacity that can satisfy the increasing energy demand.

In the last few years, several transition metal based oxides (TMOs) (M_xO_y; M = Fe, Co, Ni, Cu, Zn, Sn, Ti, Mn, Mo *etc.*; x and y depend on the oxide being studied) have drawn significant attention as potential anode materials, especially for high-performance LIBs, owing to their low cost, easy synthesis, and relatively high theoretical capacities.[4–16] Similarly, interest in anodes fabricated from transition metal sulfides (TMSs) (M_xS_y; M = Zn, Sn, Cu, Ni, Fe, Mo *etc.*) has also grown owing to their more promising physical and electrochemical properties, higher storage capacity, and better conductivity in comparison to the oxides.[3,15,17–26] Zn-oxide and sulfide are favourable for energy applications owing to the fact that they are low cost, non-toxic, highly stable both thermally and chemically, and easy to synthesize using different deposition techniques.[16,27–29] Apart

[a]*Department of Materials Science and Engineering, Optoelectronics Convergence Research Center, Chonnam National University, Gwangju 61186, Republic of Korea. E-mail: jheo@jnu.ac.kr*

[b]*School of Chemical Engineering, Chonnam National University, Gwangju 61186, Republic of Korea*

[c]*School of Materials Science and Engineering, Yeungnam University, 214-1, Dae-dong, Gyeongsan-si 38541, Republic of Korea*

† Electronic supplementary information (ESI) available: Cross-sectional FIB-SEM images of ZnOS on a SS substrate, dQ/dV plots and charge–discharge profiles of ZnOS75, ZnOS150, pristine ZnO and ZnS anodes, capacity comparison between ZnOS40 and ZnOS50, comparative plots for coulombic efficiency and specific capacity retention of ZnOS50, ZnO and ZnS electrodes, SEM images of as-deposited ZnO and ZnS anodes, post-cycling *ex situ* XRDs, and a table comparing the performance of existing ZnO, ZnS and ZnOS anodes in LIBs with that in the present work. See DOI: 10.1039/c8ta04129f

from other applications, these materials show excellent energy storage performance as anodes for LIBs. Electrochemical reactions result in formation of several alloys between Li and Zn (such as $LiZn_4$, Li_2Zn_5, $LiZn_2$, Li_2Zn_3 and LiZn)[30–32] that exhibit a high theoretical capacity (>900 mA h g^{-1}) of these materials.[3,4,14,19] However, the application of Zn-based oxide and sulfide anodes is restricted due to the continuous volume expansion and contraction during Li-ion insertion/extraction processes. This significant change in volume makes the electrode material structurally unstable, resulting in a huge loss in capacity for long cycling performance due to the low conductivity. Several efforts have been made to improve the capacity and achieve a long cycling life including morphological modification, doping with different elements, addition of conductive agents, and use of three dimensional conducting networks.[3,14,16,17,27–29,33,34] Some recent studies have demonstrated that the performance of these anodes can be improved by the addition of conductive carbon or carbonaceous additives; however, the performance of pure materials has not yet meet the standards required.[4,16,17,28,34–37] The direct growth of electrode materials onto a current collector without any binder or conductive additives will always provide an easier method for electrode fabrication and may lead to a better understanding of the electrochemical responses of the pristine material and Li-ions. Beyond binary anode materials, it has already been reported that ternary materials offer some further advantages such as a greater ability to absorb volume changes and reversible reactions with large amounts of Li, which is difficult to attain in a single system. In this regard, a few ternary double-cation anode materials, such as ZnO–SnO_2, ZnO–CoO, $NiCo_2O_4$, $ZnCo_2O_4$, and NiO–ZnO, have been shown to perform better in LIBs than their individual pristine counterparts.[38] Analogous to the double-cation system, an improvement in electrochemical performance can also be observed for double-anion-based anode materials, as reported in the existing literature for BiOF, NbOF, FeOF, due to the reversible conversion reaction.[39–41] This increases the interest in the application of Zn-based oxysulfide (ZnOS) as a double-anion based anode material in LIBs, due to the expectation of a better performance than pristine ZnO and ZnS anodes.

Zinc oxysulfide (ZnOS) is a very well-known material in the field of photovoltaics, where it is applied as a non-toxic buffer layer in thin film solar cells, as it has several properties that can be controlled by adjusting the composition.[42–45] Various techniques have been used to deposit ZnOS films; these include chemical spray pyrolysis,[45] chemical bath deposition (CBD),[46] sputtering,[42,47,48] pulsed laser deposition (PLD),[49–51] and atomic layer deposition (ALD).[44,52–55] However, besides its solar cell applications, this material has not been widely explored in the field of energy-storage devices. To the best of our knowledge, Xu *et al.* have produced the only report on PLD-ZnOS thin film anodes in LIBs,[51] which showed an enhanced electrochemical behaviour in comparison to ZnO and ZnS anodes.

Atomic layer deposition, a self-limiting sequential gas-phase deposition technique, has already been proven to be capable of achieving uniform, conformal, and pinhole-free thin film growth, with a precise control of the film thickness down to the Angstrom level on any randomly oriented substrate. Owing to its various advantages, the ALD process has widely been used to deposit several oxide[4,13,16,56] and sulfide[25,26,57–61] based materials. Interestingly, a combination of oxide and sulfide ALD processes could successfully lead to the possible deposition of metal oxysulfides with precise control. Therefore, along with several binary materials, ALD has also exhibited its potential for ternary thin film deposition compared to other deposition processes. This is because of the easily and finely tunable stoichiometry of the constituent components by tailoring the precursor pulse ratio during the deposition process.[43,44,54]

In recent years, the advantages of ALD imply that it has seen widespread use in different fields of energy applications, including energy storage devices such as batteries. The continuing decrease in the size of microelectronic devices demands energy storage systems with favourable dimensions, such as 3D microbatteries, where ALD is a promising technique for the precise deposition of thin film electrodes on high aspect ratio substrates. Therefore, the development and adoption of ALD are essential for the fabrication of battery active materials, such as cathodes, anodes, and solid-state electrolytes. In the past few years, rapid progress has been made in this field due to the application of ALD that includes a thin protective layer (such as Al_2O_3, TiO_2, and ZrO_2) on active materials. This includes cathodes, anodes, and solid-state electrolytes as well as two and three dimensional electrodes, especially for LIBs and Na-ion batteries (SIBs).[13,16,25,26,34,56,60,62–65]

In this work, we explore the electrochemical performances of thin ALD-ZnOS films against lithium. We used sequential exposure of diethylzinc (DEZ) and H_2O/H_2S to deposit ZnOS films on a stainless steel (SS) current collector and carried out coin cell fabrication with no further post-deposition processing to create carbon and binder-free anodes for LIBs. The film growth rate was studied using *ex situ* ellipsometry and X-ray reflectivity (XRR) measurements. The crystallinity, elemental composition, and surface morphology of the as-deposited films were investigated using X-ray diffraction (XRD), transmission electron microscopy (TEM), X-ray photoelectron spectroscopy (XPS), and scanning electron microscopy (SEM). A comparative electrochemical study was carried out for thin ZnOS films with different thicknesses. Increasing the thickness/mass loading of the active ZnOS material led to a decrease in the specific capacity. A significant improvement in the specific capacity and long cycling stability of the ZnOS anode compared to pristine ALD-grown ZnO and ZnS anodes was demonstrated at a higher current rate than that previously reported.[51] Thus, we have established, with experimental evidence and scientific explanations, that the presence of more electrochemically active S in the ALD-ZnOS films results in a higher stable capacity with minimal capacity fading due to the more conductive nature of these O-rich ZnOS films.

2. Experimental

2.1 Deposition of electrode materials

We opted to use ALD for the deposition of thin zinc oxysulfide (ZnOS) films using a laminar-flow-type thermal reactor (NCD,

Lucida D100, Korea), with a substrate temperature of 120 °C. Thin ZnOS films were deposited with alternative ALD cycles of ZnO and ZnS, where DEZ (LG Chem., Korea) was the common precursor for Zn and the reactants for the oxide and sulfide were DI-H_2O and 10% hydrogen sulfide (H_2S mixed with N_2; Gaschem., Korea) gas, respectively (Fig. 1). The DEZ and H_2S sources were kept at room temperature, while the H_2O source was kept at 10 °C throughout the deposition process. A continuous flow of N_2 at 50 sccm was used for purging and as the carrier gas during the ALD process. One ZnO ALD cycle comprised a DEZ pulse (0.2 s), N_2 purge (10 s), H_2O pulse (0.2 s), and N_2 purge (20 s); for one ZnS cycle, the H_2O pulse was replaced by a H_2S pulse, followed by a 10 s N_2 purge. Detailed investigations on the deposition and properties of thin ZnOS films with different pulse sequences of ALD precursors can be found elsewhere.[54] In this study, we applied different numbers of ALD supercycles, 50, 75, and 150, to obtain thin ZnOS films with different thicknesses, where one supercycle consisted of nine ALD cycles of ZnO and one of ZnS. Henceforth, these electrodes will be named ZnOS50, ZnOS75, and ZnOS150, respectively. The ZnO and ZnS ALD cycle ratio of 9 : 1 was kept constant for all of the film depositions. The pristine ZnO and ZnS thin films were also deposited under the same conditions for comparison. The thin films were deposited on Si for thickness measurements and on SS substrates for thickness measurements, different material characterizations, and battery applications. The SS substrates were cleaned with a soap solution, followed by 10 min of sonication in acetone and then in DI-H_2O; finally, they were dried with N_2 prior to the ALD process.

2.2 Material characterization

The thickness, roughness, and mass density of the as-deposited films on Si reference substrates were obtained from the XRR (PANalytical, X'Pert Pro MRD) measurements, where X'Pert reflectivity software was utilized to simulate a curve fitted to the experimental data. The thicknesses of the films grown on the Si substrates were verified by ellipsometry (Gaertner, Stokes Ellipsometer LSE). Glancing angle X-ray diffraction (GAXRD, $\omega = 0.5°$) was carried out to probe the crystallinity of the as-deposited films on SS substrates using a high resolution X-ray diffractometer (PANalytical, X'Pert PRO MPD, equipped with Cu Kα radiation of 1.542 Å). The chemical compositions of the as-deposited films on the SS substrates were investigated by XPS analysis with a VG Multilab 2000 X-ray photoelectron spectrometer using an Al Kα source. The surface morphology characterization and the energy-dispersive spectroscopy (EDS) elemental mapping of the as-deposited and post-electrochemical cycling films on the SS substrates were performed with plan-view SEM imaging using a field emission scanning electron microscope (FESEM, Hitachi SU-70, Schottky field emission type electron gun (ZrO/W emitter)). Cross-sectional TEM and EDS (JEOL, JEM-2100F equipped with 200 kV field emission gun) analyses were carried out to investigate the structural and elemental distribution of ALD-grown ZnOS films. The focused ion beam (FIB) lift-out technique was used to prepare the sample for cross-sectional TEM analysis.

2.3 Coin cell fabrication and electrochemical studies

Electrochemical studies of the ALD-grown electrode materials were carried out in CR2032 coin-cells at room temperature. All the thin films were deposited on a 16 mm diameter SS-disk current collector, which was used directly as the working electrode, with no binder or conductive additives and without any post-deposition treatment (Fig. 1). Metallic Li foil was used as the counter/reference electrode against the ALD-grown active material for the fabrication of LIBs. An Ar-gas filled glove box was used to assemble the coin cells. A porous polypropylene (PP) (Celgard 3401) separator was used to separate the electrodes with 1 M $LiPF_6$ in 1 : 1 (vol) ethylene carbonate/dimethyl carbonate (EC/DMC) as the electrolyte. The cyclic voltammetry (CV) measurements were performed within the potential window of 0.01–3.0 V *vs.* Li/Li^+ with a scan rate of 0.2 mV s^{-1}, and electrochemical impedance spectroscopy (EIS) in the frequency range of 200 kHz to 0.01 Hz was carried out for all the cells using an SP-150 (Biologic, France). The galvanostatic charge–discharge performances were investigated using a WBCS 3000 (Won-A-Tech, Korea) battery testing unit in the same potential range at different current densities. The mass loading of the active material for each electrode on the SS current collector was estimated using the thickness of the ALD-grown thin films as measured on the Si substrates which were deposited during the same reaction process. The density was calculated for each of the materials

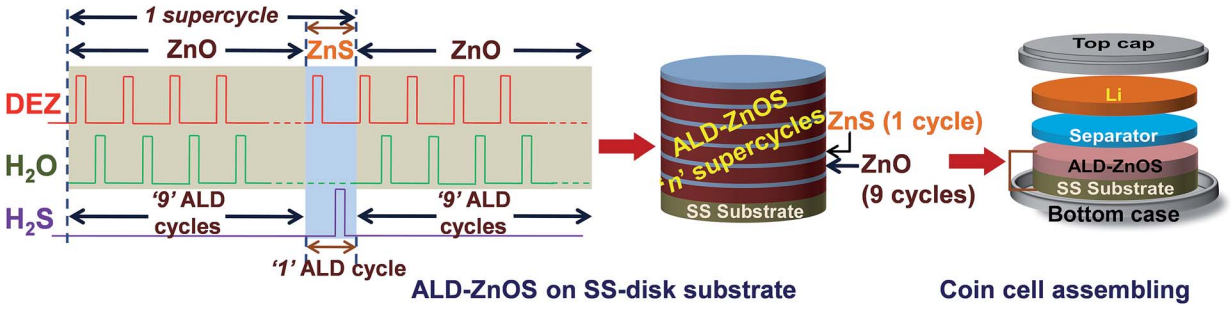

Fig. 1 Schematic representation of the precursor pulse sequence used for ZnOS thin film deposition by ALD on a SS substrate, followed by its direct use as a carbon and binder-free electrode in a coin cell LIB.

and was used for the mass calculations as obtained from the XRR measurements.

3. Results and discussion

3.1 Material characterization

For the XRR measurements, the films were deposited on Si substrates at 120 °C using 300 ALD cycles for pure ZnO and ZnS, and 30 supercycles for ZnOS. Experimentally obtained Kiessig fringes and a fitted curve for a suitable model of the film stack, as shown in Fig. 2a, were utilized to evaluate the properties of the film such as thickness, roughness, and density. The thicknesses of the ZnO, ZnS, and ZnOS thin films were calculated to be 44, 34, and 42 nm, respectively, based on the XRR measurements; the corresponding average growth rate per cycle (GPC) were ~1.5, 1.1, and 1.4 Å per cycle, respectively. The mass densities of the ALD-grown ZnO, ZnS, and ZnOS thin films were found to be ~5.58, 4.00, and 4.81 g cm^{-3}, and these results were used to estimate the mass loading on the SS current collector during the electrochemical characterization. The GPC of all the ALD thin films was also verified using ellipsometry measurements on the Si substrates. In addition, since the films were deposited on SS substrates for the electrochemical studies, the GPC of the ALD grown film was also verified using cross-sectional FIB-SEM imaging, as shown in Fig. S1 (ESI).† The ZnOS film deposited using 300 ALD supercycles on the SS substrate had a thickness of ~428 nm, which corresponded to a GPC similar to the 1.4 Å per cycle obtained from the XRR and ellipsometry measurements on the Si substrates. This confirms that the growth rates of the films are similar, irrespective of the substrate.

XRD patterns of the as-deposited films on the SS substrates and the bare SS substrate were obtained using the glancing incidence angle ($\omega = 0.5°$) configuration for 2θ values ranging from 25 to 70° and are shown in Fig. 2b. It can be clearly seen from the figure that the as-deposited ZnO film is polycrystalline in nature, with all the peaks consistent with those of the hexagonal wurtzite structure (JCPDS ref. 00-036-1451). On the other hand, the XRD pattern of the thin ZnS film exhibited only one high intensity peak at ~28.5° which corresponds to the (111) or (002) plane of cubic (JCPDS ref. 00-001-0792) or hexagonal ZnS (JCPDS ref. 00-036-1450).[53] When one ZnS cycle was incorporated into the ZnO cycle, the intensities of the ZnO peaks decreased and shifted to lower angles, as observed from the XRD pattern of the thin ZnOS film.[48,53,54] It should be noted that the ionic radius of S is larger than that of O,[48,66] and therefore, the lattice constant increases due to the incorporation of S into the ZnO lattice, which caused a decrease in the diffraction angle during the XRD analysis of ZnOS.

XPS measurements were performed for the ALD-grown ZnO, ZnS, and ZnOS thin films on the SS substrate to investigate the chemical compositions. The full XPS survey spectrum, in the binding energy range of 0–1200 eV, presents the constituent elements of the individual films, as shown in Fig. 2c. For a detailed study, the XPS spectra corresponding to each element in the high resolution energy scan are shown in Fig. 2d–f. The

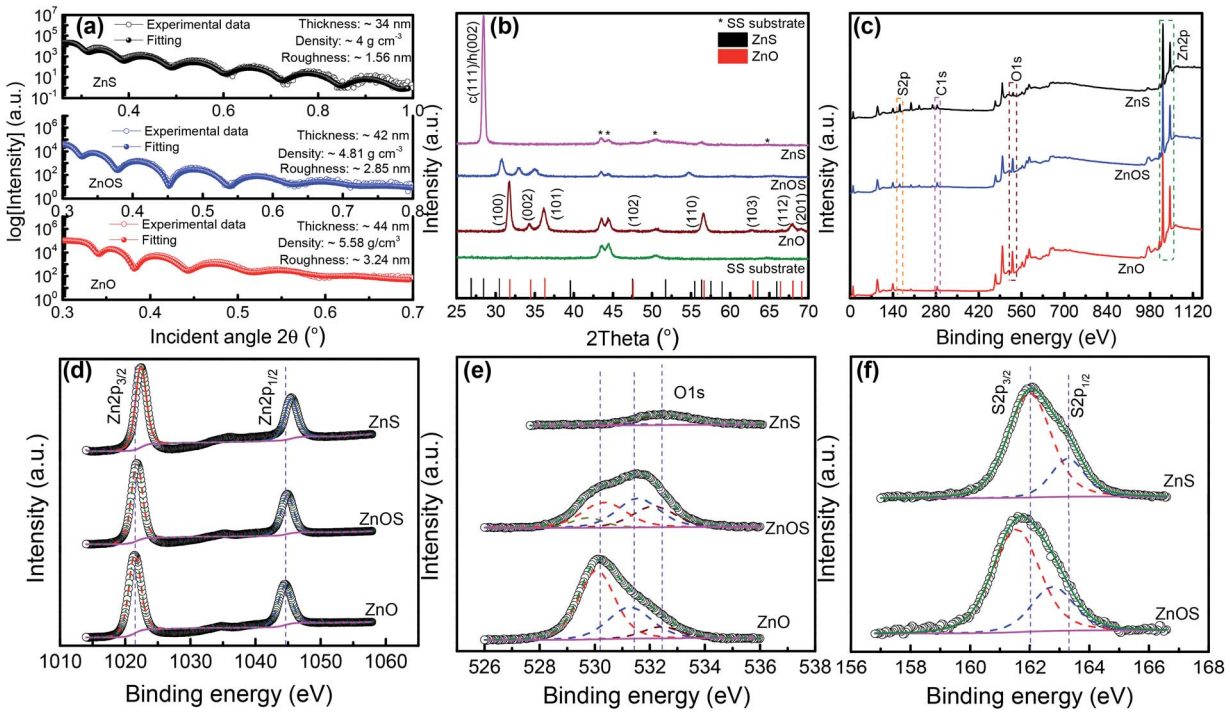

Fig. 2 (a) Measured and fitted Kiessig fringes from the XRR measurements of ZnO, ZnS, and ZnOS on Si-substrates with the calculated thickness, mass density, and roughness of the deposited films; (b) glancing angle XRD patterns (the lines in the bottom panel show the powder diffraction patterns of ZnO and ZnS); (c) XPS full survey and individual XPS spectra of (d) Zn 2p, (e) O 1s, and (f) S 2p of the as-deposited ALD-grown ZnO, ZnS, and ZnOS thin films on SS substrate showing the crystallinity and elemental composition, respectively.

Zn 2p XPS peaks corresponding to ZnOS, as seen in Fig. 2d, show Zn $2p_{3/2}$ and Zn $2p_{1/2}$ doublets at binding energy values of 1021.8 and 1044.9 eV, respectively,[44,45] which are approximately the same as the binding energies of the Zn^{2+} oxidation state of ZnO (1021.45 and 1044.55 eV, respectively).[16,67] On the other hand, the Zn 2p spectrum of ZnS shows the Zn $2p_{3/2}$ and Zn $2p_{1/2}$ peaks at higher binding energies of 1022.45 and 1045.5 eV which are approximately the same as those in previous reports.[17,68] Thus, the binding energies in the Zn 2p spectrum of ZnOS were consistent with those of ZnO, irrespective of the S incorporation, which indicates the same Zn^{2+} oxidation state.

Fig. 2e shows the XPS O 1s spectrum of the three different materials with possible peak fittings. The O 1s spectrum of ZnOS is fitted with four peaks centered at 529.9, 530.3, 531.5, and 532.3 eV. Among these, the fitted peak with a binding energy of 530.3 eV is attributed to the lattice oxygen of the Zn–O bonds in the wurtzite ZnO structure, which also correlates with the O 1s spectra of pristine ZnO.[16,45,67] The presence of this peak suggests that there is no significant change in the ZnO lattice even after the incorporation of S. A lower binding energy peak at 529.9 eV with low intensity signifies the lower charge on oxygen, which is possibly due to the sharing of the lattice between oxygen and sulfur atoms, as reported by Thankalekshmi *et al.* for thin ZnOS films synthesized by chemical spray pyrolysis.[45] The two other peaks, fitted at the higher binding energy values of 531.5 and 532.3 eV, usually reveal an O^{2-} deficiency and the presence of chemisorbed or hydroxyl oxygen on the film surface, respectively.[12,67,69] Similar peaks are also present in the case of ZnO, while the small peak at 532.3 eV can be observed in the O 1s spectra of pristine ZnS, corresponding to the chemisorbed or hydroxyl oxygen on the film surface due to the exposure to the air atmosphere.[3] In conclusion, the XPS analyses confirm that the ALD-ZnOS films were successfully grown and lie in the O-rich region.

The S 2p spectra of ZnS and ZnOS are shown in Fig. 2f and are deconvoluted into two peaks. The doublet of S 2p peaks centered at 162.8 and 161.6 eV can be denoted as S $2p_{1/2}$ and S $2p_{3/2}$ of ZnOS, respectively, with reference to the peaks of pristine ZnS at binding energies of 163.2 and 162 eV.[17,44,45] This small shift in the peaks towards lower binding energies for ZnOS indicates a reduction in the charge on the S atoms in the mixed sulfur–oxygen matrix, where the lower energy peak at 161.6 eV is attributed to the Zn–S bond.[45] From the XPS analysis, an O/(O + S) ratio of ~0.7 was obtained for the ZnOS film deposited by using a ZnO : ZnS cycle ratio of 9 : 1.[54]

Fig. 3a–c show the plan-view SEM images of the ZnOS films deposited with increasing ALD supercycles on the SS substrates that were used for battery applications. A highly uniform film deposition across the surface area without any definite morphology can be seen from the SEM images (inset shows the low magnification images) which proves the uniform and conformal deposition by ALD. However, the SEM images clearly exhibit a microstructural change between the films. As the film thickness increased, the grains increased in size and coalesced resulting in a denser film deposition. It can also be observed from the inset images that a three-dimensional flake type structure started to grow as the film thickness increased, which can also be found for several other ALD-grown materials.[70,71] The EDS elemental mappings clearly reveal the uniform distribution of Zn (Fig. 3d), O (Fig. 3e), and S (Fig. 3f) across the surface area.

Cross-sectional TEM analysis was carried out for the ZnOS75 thin film, and the results are shown in Fig. 4, along with TEM-EDS elemental mappings. Fig. 4a shows a very uniform and conformal deposition of the ZnOS thin film with a thickness of ~100 nm, which corresponds to a GPC of ~1.3–1.4 Å per cycle supporting the XRR and ellipsometry measurements. The HRTEM micrograph in Fig. 4b reveals the polycrystalline nature

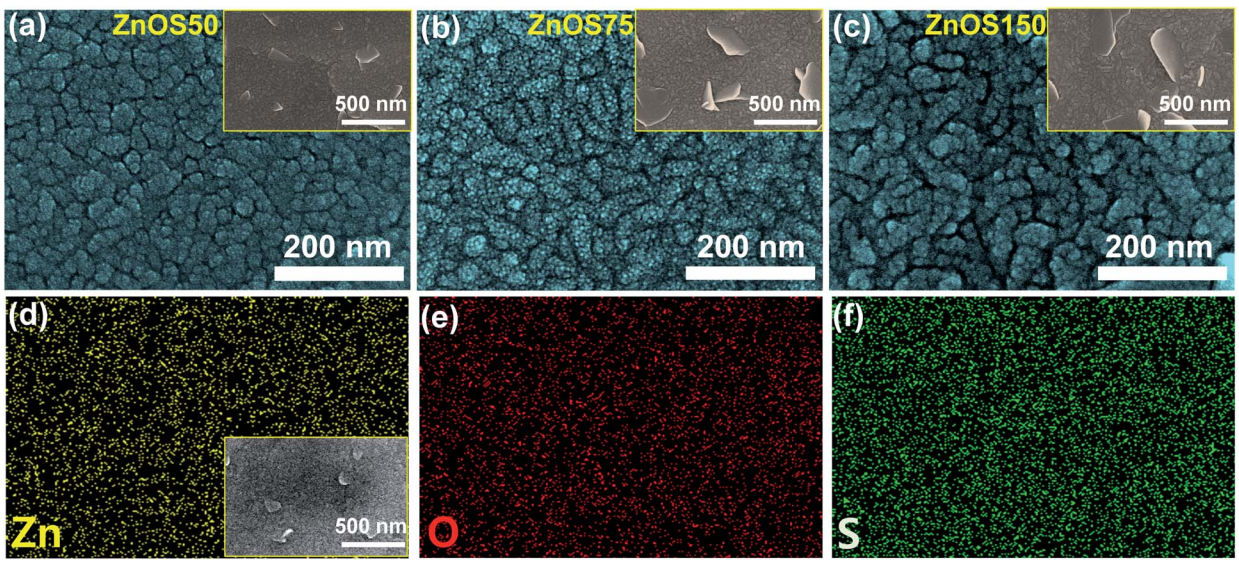

Fig. 3 Plan-view FESEM images of ALD-grown (a) ZnOS50, (b) ZnOS75, and (c) ZnOS150 films on SS substrates. Insets show the corresponding images at low magnification. EDS elemental mappings exhibit the uniform presence of (d) Zn, (e) O, and (f) S in the as-deposited ZnOS film.

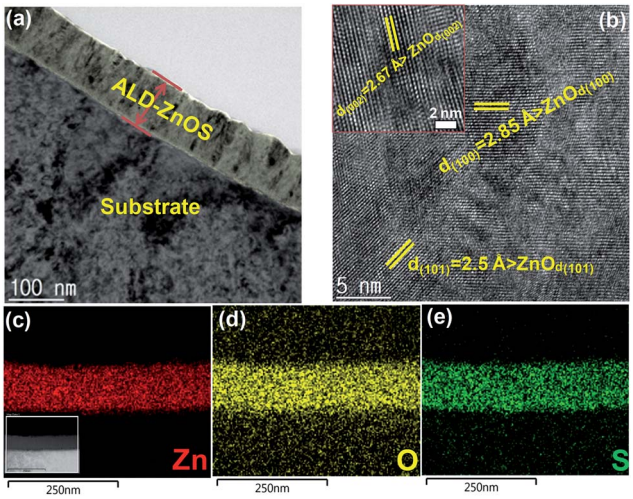

Fig. 4 (a) Cross-sectional TEM image, (b) HRTEM image showing the uniform and highly crystalline growth of the ALD-ZnOS, (c–e) TEM-EDS elemental mappings of the ZnOS film proving the uniform distribution of Zn, O, and S as the constituent elements, respectively (inset of (c) shows the TEM image for the corresponding TEM-EDS elemental mapping).

of the ZnOS thin film. From the lattice fringes, the measured interplanar spacing was found to be ~2.85, 2.67, and 2.5 Å which are slightly higher than those of the pristine ZnO wurtzite structure corresponding to the (100), (002), and (101) planes (JCPDS ref. 00-036-1451), respectively.

A small shift in the peaks of the XRD pattern to lower angles was already observed for the ZnOS film due to the increase in the lattice constant following the incorporation of S into ZnO—this also conforms to the results of the TEM analysis. Fig. 4c–e show the corresponding cross-sectional TEM-EDS elemental mappings of the ZnOS thin film. A clear and uniform distribution of the constituent elements Zn, O, and S can be observed from Fig. 4c, d, and e, respectively. Thus, the cross-sectional TEM and EDS elemental analyses exhibit the uniform and conformal deposition capability of the ALD process, even for a ternary material.

3.2 Electrochemical performances of ALD-ZnOS anodes

For all the electrochemical property studies, ZnOS films were deposited on SS current collectors and directly used as carbon and binder-free electrodes with no post-deposition processing. The thin ZnOS films with thicknesses of ~75, 100, and 215 nm were obtained by using 50, 75, and 150 ALD supercycles, respectively.

The CV measurements were performed in an applied potential window of 0.01–3.0 V (*vs.* Li/Li^+) at a 0.2 mV s^{-1} scan rate to understand the electrochemical reactions that occur in the electrodes during lithiation/delithiation processes. Fig. 5a shows the CV curves for the first five consecutive cycles obtained for ZnOS50. Following the existing literature on Zn-based electrodes,[16,27,29,51,56] the cathodic sweep of the CV includes the reduction processes where the first conversion reaction occurs to form elemental Zn from ZnOS, followed by the alloying reaction between Li and Zn. In addition, Li_2O and Li_2S matrices also form during the conversion reactions that act as buffer layers for the Li–Zn alloying and dealloying reactions. The anodic sweep comprises the reverse reaction fabricating the initial electrode material after the dealloying process. Thus, the electrochemical reactions of ZnOS in the half cell configuration can be represented as follows:[51]

Cathodic reactions:

$$ZnOS + 2Li^+ + 2e^- \rightarrow Zn + Li_2O + Li_2S \quad (1)$$

$$Zn + Li^+ + e^- \rightarrow LiZn \quad (2)$$

Anodic reactions:

$$LiZn \rightarrow Zn + Li^+ + e^- \quad (3)$$

$$Zn + Li_2O + Li_2S \rightarrow ZnOS + 2Li^+ + 2e^- \quad (4)$$

A strong reduction peak at 0.75 V can be attributed to the decomposition of ZnOS due to its reaction with Li^+ resulting in the formation of elemental Zn (eqn (1)), which is further converted into the Li–Zn alloy (eqn (2)) through several steps [$LiZn_4$ → (Li_2Zn_5 → $LiZn_2$) → Li_2Zn_3 → LiZn] reflected by the small shoulder peaks at 0.54, 0.43 and 0.08 V in the first cathodic sweep of the CV curve.[32] The main peak also includes the reduction of the organic electrolyte and the subsequent formation of a solid electrolyte interphase (SEI) that contains organic constituents such as ethylene oxide based oligomers, LiF, $LiCO_3$ and lithium alkyl carbonates.[72] On the other hand, during the first charging (anodic) process four oxidation peaks can be observed below 1 V at ~0.27, 0.35, 0.53, and 0.68 V which indicate the multistep dealloying process of the Li–Zn alloy where LiZn → Li_2Zn_3 → $LiZn_2$ → Li_2Zn_5 → $LiZn_4$ to form elemental Zn (eqn (3)).[32] The broad peak centered at a potential value of ~1.2 V is associated with the reformation of Zn to ZnOS (eqn (4)).[16,51] In the second cathodic cycle, the peak at 0.75 V disappeared and a new peak appeared at ~0.9 V, corresponding to the conversion reaction of ZnOS to Zn; this may be due to the stabilization of the electrode reactions.[16,51,72] Similarly, three prominent reduction peaks at ~0.68, 0.43, and 0.08 V corroborate the multistep alloying processes of the Li–Zn alloy. The difference between the first and the second reduction cycle can be attributed to the capacity loss after the first cathodic reaction. There were no such changes in the positions of the oxidation peaks during the anodic sweep. From the second cycle onwards, the CV curves were approximately superposed in shape, which reveal the reversible electrochemical reactions during further consecutive cycles. Similar electrochemical reaction profiles can also be observed for the ZnOS75 and ZnOS150 electrodes as shown in the dQ/dV plots (Fig. S2a and b†) for the first six consecutive cycles. Thus, all the electrochemical reaction profiles revealed well-defined reversible electrochemical reactions for the ALD-ZnOS thin films.

The electrochemical behavior of the ALD-grown ZnOS thin film anode with Li was further investigated using the galvanostatic charge–discharge process at a current density of 1 A g^{-1} within the potential window of 0.01–3.0 V. Fig. 5b shows the

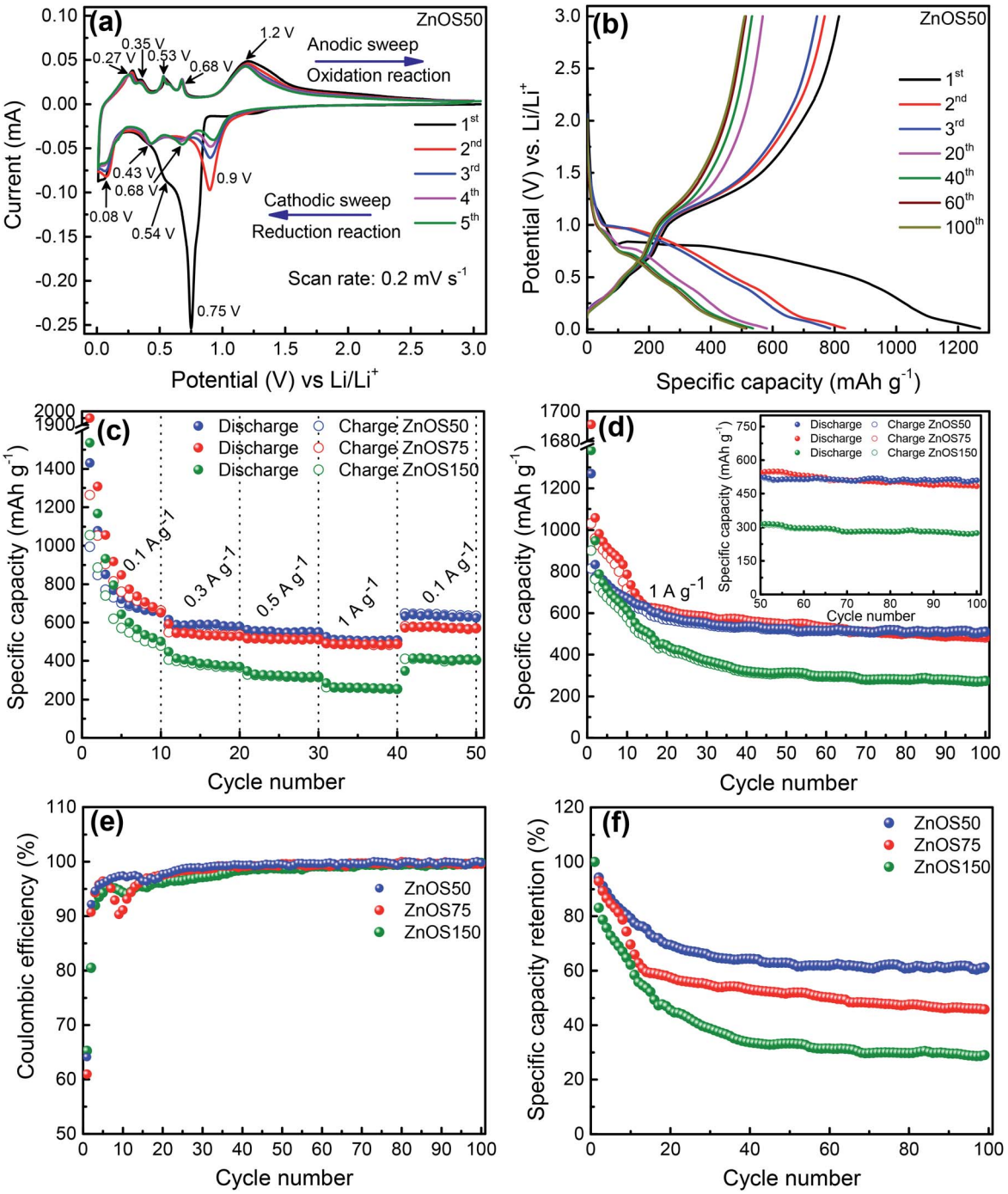

Fig. 5 Electrochemical studies in LIBs: (a) CVs for the first five consecutive cycles of ZnOS50 at a 0.2 mV s^{-1} scan rate within the potential window of 0.01–3.0 V, (b) charge–discharge profile of ZnOS50 at a current density of 1 A g^{-1} (~40 μA cm^{-2}), (c) rate capability comparison with a large variation in current density, (d) cycling performance, (e) coulombic efficiency, and (f) specific capacity retention comparison for 100 charge–discharge cycles at a current density of 1 A g^{-1} between the ALD-grown ZnOS50, ZnOS75, and ZnOS150 electrodes.

charge–discharge profile of the ZnOS50 electrode for different cycle numbers. The charge–discharge profiles of other ZnOS electrodes (ZnOS75 and ZnOS150), also obtained at the same current density and the potential window, are shown in Fig. S2c and d,† respectively. The plateaus in the voltage profiles correlate with the cathodic and anodic peaks observed in the CV curves. It can be observed that for all of the ZnOS thin films a plateau appears at ~0.8 V during the first discharge process, with small slopes in the lower potential region attributed to the electrochemical reactions between ZnOS and Li^+ to form Li–Zn alloys and the SEI layer. After the first cycle, the value of this slope is shifted to a higher potential (~0.9 V), with several small slopes at ~0.7, 0.4, and 0.1 V that correspond to the results of the CV measurements. On the other hand, the charging curves

contain small slopes in the potential region between ~0.3 and 0.7 V, with a broad slope above 1 V; this indicates the multistep dealloying process of the Li–Zn alloy and the reformation of ZnOS, respectively. The charge–discharge curves are similar in nature for the long cycling process which signifies more reversible electrochemical reactions. A very high specific capacity of 1270.6 mA h g^{-1} was obtained for the first discharge process for ZnOS50 which is explained by the formation of the SEI layer during the discharge cycle which also consumes some Li^+.[27,73] The first charge capacity was 814.4 mA h g^{-1}, which lead to a coulombic efficiency of 64.1% in the first cycle. The formation of the SEI layer, decomposition of the electrolyte, and other irreversible processes involved in the first cycle are possible causes for the irreversible capacity loss, which can also be found for other metal oxide-based anodes.[12,51,72] The similarity of the potential curves in the subsequent cycles is attributed to the reversible reactions that occur upon cycling. A similar charge–discharge behavior was observed for all the ALD-ZnOS anodes with different film thicknesses.

The rate capabilities of the ALD-grown ZnOS thin film electrodes were studied at different current rates over 10 cycles each in the same potential range between 0.01 and 3.0 V, as shown in Fig. 5c. Of the three electrodes, ZnOS50 shows the highest and most stable specific capacity. A high first discharge capacity of 1430.5 mA h g^{-1} was obtained for the ZnOS50 electrode at a current density of 0.1 A g^{-1}, which reached 650.3 mA h g^{-1} at the end of the tenth cycle, following a significant capacity drop as the charge–discharge cycle number increased. The current density was then gradually increased up to 1 A g^{-1}. The ZnOS50 electrode showed only a slight capacity drop and was highly stable as the current density increased. The first discharge cycle capacity values for the ZnOS50 electrode were 614.5, 562.8, and 525.6 mA h g^{-1} at current densities of 0.3, 0.5, and 1.0 A g^{-1}, respectively. When the current density returned to its initial value of 0.1 A g^{-1}, the ZnOS50 electrode recovered a specific capacity value of 632.9 mA h g^{-1}, ~97.3% capacity retention with respect to the 10^{th} cycle of the initial 0.1 A g^{-1} current density, while the ZnOS75 and ZnOS150 electrodes showed 87.5 and 69.4% recovery in capacity, respectively. This study indicates the reversibility and stability of the ALD-ZnOS thin film anodes for use in LIBs at different current densities. However, there was only a slight difference between the specific capacities and stability of the ZnOS50 and ZnOS75 electrodes, while the ZnOS150 exhibited a relatively unstable behavior with the capacity fading rapidly with the increasing charge–discharge cycle number at different current densities.

The long cycling performances of the ZnOS electrodes were recorded for the detailed study of the stability and specific capacity with the varying film thickness. Fig. 5d compares the cycling stability of the ZnOS anodes of different thicknesses for 100 charge–discharge cycles, within 0.01–3.0 V, at a constant current density of 1 A g^{-1}. The first discharge capacities of 1270.6, 1691.1, and 1381.4 mA h g^{-1} and charge capacities of 814.4, 1030.6, and 901.4 mA h g^{-1} were obtained for ZnOS50, ZnOS75, and ZnOS150, respectively. The high discharge capacity and lower coulombic efficiency (~61–65%) were mainly the consequences of the SEI layer formation and the irreversible reactions occurring during the first cycle, as mentioned previously. After the first cycle, a gradual decrease in the capacity was observed for all of the electrodes with different fading rates (Fig. 5f); however, the electrochemical reactions were reversible, as indicated by the considerable increase in the coulombic efficiency (Fig. 5e). After a few initial charge–discharge cycles, the capacities were approximately stable with no significant fading until 100 cycles (inset of Fig. 5d). From the figure, it can clearly be seen that while the ZnOS50 anode showed very quick and excellent stability up to 100 cycles compared to ZnOS75, a continuous capacity decay was observed for ZnOS150 over a large number of cycles. After 100 cycles, the stable specific discharge capacities of 510.3, 484.7, and 275.0 mA h g^{-1} with a very high coulombic efficiency of ~99% were achieved by the ZnOS50, ZnOS75, and ZnOS150 anodes, respectively. Thus, it is found that the most stable electrochemical performance was obtained for the ZnOS50 anode with a high capacity retention of ~61% after 100 charge–discharge cycles with respect to the second cycle discharge capacity in comparison with ~46 and 29% for ZnOS75 and ZnOS150, respectively (Fig. 5f). From these results, we observe that the thickness of the electrode material (mass loading) has a significant influence on the electrochemical performance of LIBs, demonstrated by the increase in capacity fading with the increase in film thickness/higher mass loading, which resulted in a decrease in the stable specific capacity.[4,13,74] However, there might be scope to achieve higher capacity for the electrodes grown with less than 50 ALD supercycles, further. The thinnest film (ZnOS50) in this particular case yields a thickness of ~75 nm which further corresponds to ~43 μg cm^{-2}. The mass was measured by weighing the SS-disk substrate before and after deposition and compared with the theoretical mass that was estimated from the volume and mass density of the ALD-grown film. Any lower mass loading than this might result in a significant over/under-estimation in the capacity, and therefore we would like to recommend 50 ALD supercycles as the threshold condition for this ZnOS electrodes. Moreover, the specific capacity should not vary much even if we go further lower than 50 supercycles which is reflected from the cycling performance of ZnOS50 and ZnOS75. To ensure this, a careful experimentation with 40 ALD supercycles (ZnOS40) was further carried out which revealed almost same stable specific capacity at the end of 100 charge–discharge cycles. Fig. S3† shows the comparative cycling performance of ZnOS40 and ZnOS50 at 1 A g^{-1} current density. The irreversible capacity fading during the initial cycles is usually because of the low conductivity and a lack of structural stability. The increase in the internal resistance is a possible reason for the capacity loss in the thicker films, as it could result in an over-potential which may result in several side reactions during the electrochemical cycles.[74–76] On the other hand, such capacity fading may also be associated with the mechanical stability of the electrode material. A significant change in the volume of the electrode material generally occurs through the Li^+ insertion and de-insertion process during the charge–discharge cycle. The volume change creates a strong internal stress which leads to the pulverization and strong polarization of the electrode material.[4,28,56] The internal stress accumulates more within the

thicker films as it is harder to release; this induces severe mechanical instability. This instability may enhance the formation of cracks or fractures in the electrode material that subsequently decrease the stable capacity due to the loss of contact with the current collector during the long cycling performance.[4,13,74,77,78] Alternatively, the capacity loss of the thicker films could also result from the Li-ion diffusion limited process within the electrode material which is a function of film thickness at a constant current density. The surface of the active material at the electrode boundary becomes electrochemically inactive when the electrode thickness is higher than the characteristic diffusion length. As a consequence, a significant decrease in the capacity can be observed as electrochemical reactions occur only at the electrode surface which is not usually electrochemically active for longer cycling processes at high current rates.[74,79,80]

To gain further insights into the kinetics and electrochemical performance of the ZnOS anodes, EIS measurements were performed before and after 100 charge–discharge cycles in the frequency range of 200 kHz to 0.01 Hz. The comparisons between the Nyquist plots of the ZnOS electrodes are shown in Fig. 6a and b, obtained from the EIS measurements before and after cycling, respectively, along with the fitted curve by using the equivalent electrical circuit model (shown in the inset of Fig. 6b). Here R_s and R_{ct} represent the electrolyte resistance and the charge transfer resistance, respectively, while CPE is the constant phase element due to the depressed semicircle in the measured data, and Z_W is Warburg impedance. A Nyquist plot of an electrochemical system can be separated into different parts; the first semicircle in the high-frequency region corresponds to the formation of the SEI layer and contact impedance at the interface between the active material and the electrolyte, and the second semicircle from high to medium frequency regions corresponds to the R_{ct} between the electrode and electrolyte. However, in some cases it is difficult to separate the two semicircles in the high-medium frequency region and a large semicircle is formed, which can be considered to be the superposition of two semicircles. In the third region of the Nyquist plot, a typical Warburg behavior is observed from the slope of the linear portion in the low frequency region of the curve; this is due to the frequency-dependent migration of alkali ions through the SEI layer and the diffusion of ions through the electrolyte. In this case, the resulting plot shows a high-frequency semicircle corresponding to the electrolyte and charge-transfer resistances at the electrode/electrolyte interface.[4,33,81] From Fig. 6a (inset shows the zoomed version) we can clearly see that the diameter of the semicircle obtained for ZnOS50 and ZnOS75 is much smaller than that of ZnOS150 which indicates a lower contact and R_{ct} along the interface for the first two, whereas ZnOS150 displays an incomplete semicircle, indicating a very high R_{ct} along the interface (Table 1). The similar charge-transfer resistance reflected for ZnOS50 and ZnOS75 before cycling is in good agreement with their close capacity values. However, these resistances increase

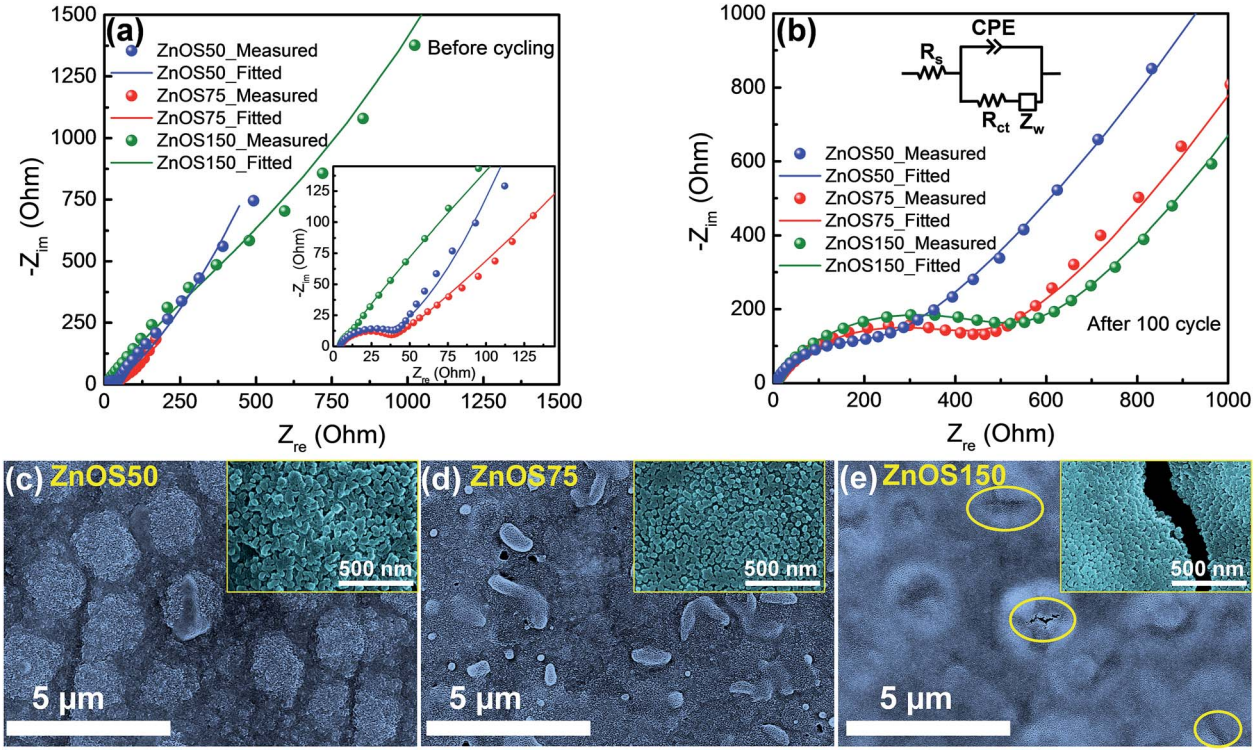

Fig. 6 Nyquist plots obtained from the EIS measurements along with the fitted curves of ALD-ZnOS electrodes with different thicknesses: (a) before and (b) after 100 charge–discharge cycles (inset shows the corresponding equivalent circuit used for the EIS measurement data fitting). Plan-view FESEM images of (c) ZnOS50, (d) ZnOS75, and (e) ZnOS150 after 100 charge–discharge cycles. Insets show the high magnification images. Yellow circles indicate crack formation in ZnOS150.

Table 1 Before and after cycling R_{ct} values of ZnOS50, ZnOS75, and ZnOS150 electrodes

Electrodes	Before cycling R_{ct} (ohm)	After 100 cycles R_{ct} (ohm)
ZnOS50	30	237.8
ZnOS75	32.1	460.6
ZnOS150	1500	524.2

considerably after 100 charge–discharge cycles, as shown in Fig. 6b where there is a considerable difference in the semicircles obtained for ZnOS50 and ZnOS75 anodes. The higher R_{ct} value (Table 1) for ZnOS75 after cycling could be easily correlated with its lower capacity retention compared to the ZnOS50. However, ZnOS150 also showed a prominent semicircle with a lower R_{ct} value after cycling in contrast to the before cycling value. This might be due to the severe deformation or large crack formation (Fig. 6e) that allows more electrolyte to come into contact with the electrode material as well as it might also come into direct contact with the SS substrate. Therefore, unlike to ZnOS50 and ZnOS75, the EIS of ZnOS150 showed an opposite trend before and after cycling. Nevertheless, ZnOS150 still has the highest R_{ct} value among all of these three electrodes even after cycling which reflects its poor performance compared to the others. These results clearly reveal that the thickness of active electrode material significantly affects the Li-ion diffusion which reduces drastically for $ZnOS_{150}$ due to its high thickness. Thus, the EIS measurements illustrated the higher conductive nature of the ZnOS50 anode which supports the theory of enhanced stable capacity when compared to the ZnOS75 and ZnOS150 anodes.

The post-cycling SEM images (Fig. 6c–e) were obtained after 100 charge–discharge cycles. The electrodes were dismantled and washed using dimethyl carbonate to remove the electrolyte salts and dried in the glove box overnight before analysis. As expected, agglomeration occurred in the films due to the large volume change during the charge–discharge process, which resulted in the formation of multiple cracks that explain the lower capacity retention of the thicker film (Fig. 6e). However, the material remained intact with the current collector after 100 cycles, indicating the robustness and stable capacity of the binder-free thin film electrodes formed by ALD.

3.3 Comparative electrochemical study of ZnOS50 with pristine ZnO and ZnS anodes

A further charge–discharge cycling study was carried out to compare the electrochemical performance of ZnOS, ZnO, and ZnS anodes. For this purpose, pristine ZnO and ZnS anodes were produced with a similar mass to ZnOS50 by adjusting the thicknesses of the ZnO and ZnS films to ~70 and 90 nm, respectively. Fig. 7a shows the comparative charge–discharge cycling performances of ZnOS50 with pristine ZnO and ZnS anodes over 100 cycles at a constant current density of 1 A g^{-1} (~40 μA cm^{-2}) in the 0.01–3.0 V potential range. This study clearly reveals that when a small amount of sulfur is incorporated into ZnO, it leads to a significant enhancement of the stable specific capacity of the ZnOS50 anode in comparison to the pristine ZnO and ZnS anodes. While ZnOS50 delivered a higher stable discharge capacity of 510.3 mA h g^{-1}, pristine ZnO and ZnS had stable capacities of 360.3 and 449.2 mA h g^{-1} after 100 cycles, respectively. The corresponding charge–discharge profiles of ZnO and ZnS are shown in Fig. S5a and b.†

The dQ/dV plots were obtained from the charge–discharge profiles in order to understand the electrochemical reactions presented in Fig. S5c and d.† It can be found from the CV of ZnOS50 and the dQ/dV profile of ZnO and ZnS that the first cycle of the cathodic and anodic sweeps is similar in nature for all of the anode materials. The strong high intense peaks represent the decomposition of the anode material to form elemental Zn and the SEI layer, along with small peaks at lower potentials due to the formation of Li–Zn alloys during the first cathodic sweep. Similarly, during the anodic sweep the dealloying process of the Li–Zn alloys is represented by the small peaks below 1 V and the peak at ~1.3 V is associated with the reformation of ZnO/ZnS. An extra peak was observed at a high potential of ~2.6 V for both the ZnO and ZnS anodes during the first anodic sweep; this is attributed to the complete reformation of ZnO and ZnS.[27,33,82] It should be noted that the same peak was observed not only for ZnOS150 (Fig. S2b†), but also for ZnOS50 and ZnOS75 at lower current density, during the first cycle (Fig. S4†). Thus, the oxidation peak at high potential was completely in line with our observations for all of the electrodes studied in this work. From the second cycle onwards, significant changes can be observed in the electrochemical performance of the pristine ZnO and ZnS anodes, which is a possible explanation for the lower performance of these anodes. The charge–discharge profile (Fig. S5a†) and dQ/dV plot (Fig. S5c†) of ZnO clearly reveal that although the peaks that appear for the dealloying process during charging remain unchanged, the peak corresponding to the reformation of ZnO at ~1.3 V started to decrease rapidly, and the peak at ~2.6 V disappeared completely after the first cycle. A similar phenomenon can be observed for the pristine ZnS anode, where the decreasing rate of the ~1.3 V peak was a little lower than that for ZnO. On the other hand, the CV and charge–discharge profile (Fig. 5a and b) show that the electrochemical reaction plateaus of ZnOS50 were quite reversible up to 100 cycles. This indicates that the increasing rate of capacity loss may be due to the irreversible reaction of ZnO/ZnS decomposition and formation in the pristine materials during the long cycling process. However, the other plateaus which correspond to alloying–dealloying reactions remain unchanged which attests that the electrochemical performance of these anodes is strongly governed by the regeneration step of ZnO/ZnS/ZnOS. Thus, this may be one explanation for the inferior performance of the pristine ZnO and ZnS anodes and the significant capacity fading observed during the initial cycles. After the first few cycles, the capacities stabilized (inset of Fig. 7a) and the coulombic efficiencies reached ~97–98% (Fig. S6a†) indicating the reversible alloying–dealloying processes only (eqn (2) and (3)), and leading to the lower specific capacity. A similar behavior was demonstrated by Xu *et al.*[51] for their pulsed laser deposited ZnOS, ZnO, and ZnS anodes in LIBs; they reported a specific capacity of ~600 mA h g^{-1} after 40 charge–discharge

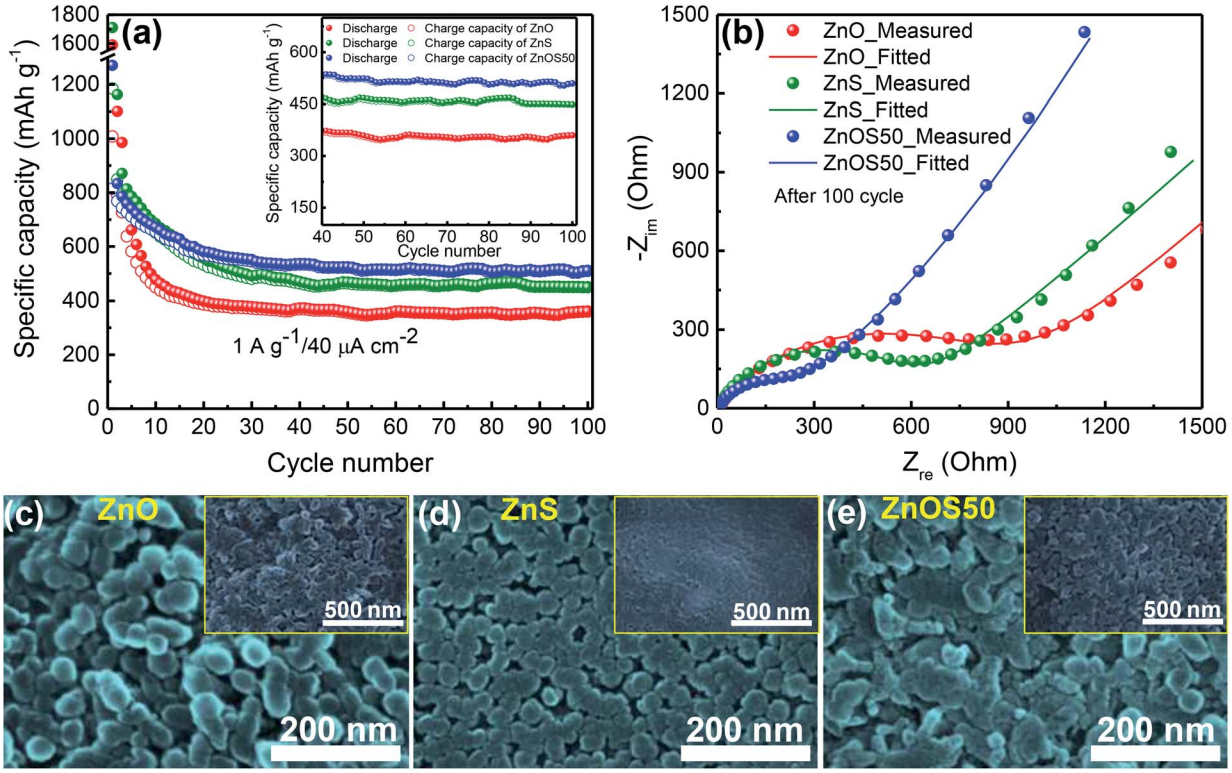

Fig. 7 Comparison between the (a) cycling performances at a current density of 1 A g^{-1} (~40 μA cm^{-2}) for 100 charge–discharge cycles, and (b) EIS measurements (Nyquist plots) and the corresponding fitting curves of the ALD-grown ZnOS50, pristine ZnO, and ZnS anodes in LIBs. Plan-view FESEM images of (c) ZnO, (d) ZnS, and (e) ZnOS50 after 100 charge–discharge cycles. Insets show the low magnification images.

cycles for S-rich ZnOS films at a very low current density of 2 μA cm^{-2}. Therefore, we believe that the current work reports a superior performance at a much higher current density (1 A g^{-1}) for O-rich ALD-ZnOS. Moreover, as mentioned earlier, the reversible capacity of ~650 mA h g^{-1} at the relatively low current density of 0.1 A g^{-1} (~4 μA cm^{-2} which is higher than the value used for PLD ZnOS) is also higher than the previously reported value. The superior performance of this present electrode could be attributed to three simultaneous factors: (a) the excellent homogeneity in the composition of ALD-ZnOS, (b) its excellent uniformity across the complete SS current collector, and (c) the precise thickness optimization (~75 nm) of the active anode material using the ALD technique.

We have already mentioned that one main reason for the initial capacity loss is the low conductivity of the active material. The increase in the internal resistance of the electrode restricts the Li-ion diffusion, which in turn deteriorates the electrochemical performance. The EIS measurements of ZnOS50, ZnO, and ZnS (Fig. 7b) after cycling clearly reveal the lowest R_{ct} value (237.8 Ω) along the interface for ZnOS50 in comparison to the pristine anode materials (R_{ct} values of ZnO and ZnS are 896.6 and 591.6 Ω, respectively), which correlates with its best performance. A slightly higher conductivity was observed for the ZnS anode, which exhibited a better performance than ZnO. However, low capacity retention was observed for both the ZnO and ZnS anodes (~36–38%) in comparison to ZnOS50 (~61%) as shown in Fig. S6b.†

On the other hand, surface SEM images of the post charge–discharge cycling electrodes (Fig. 7c–e) exhibited better structural stability in the ZnOS50 film compared to the pristine ZnO and ZnS films (before cycling surface FESEM images of ZnO and ZnS on a SS substrate are shown in Fig. S6c and d,† respectively) which were affected more by the detrimental effect of the large volume change during the charge–discharge process.

In addition, the post-cycling *ex situ* XRD analyses of ZnO, ZnS, and ZnOS50 electrodes were carried out further at a completely charged state (3.0 V) after several charge–discharge cycles to investigate the possible reaction mechanism for each of them. For this study, the electrodes were prepared by following the similar process adopted for post-cycling SEM analyses. The post-cycling *ex situ* XRD patterns are shown in Fig. S7 in the ESI.† The XRD analyses clearly showed the presence of metallic Zn at the peak position of ~36.3°, 39°, and 54.3° corresponding to the (002), (100), and (102) planes (JCPDS ref. 00-004-0831), respectively, for the pristine ZnO electrode after complete charging. It clearly reveals that ZnO undergoes an irreversible reaction with Li after the first discharge cycle, which can also be observed in Fig. S5c;† the capacity is mainly derived from the alloying reaction between Li and Zn (Li–Zn alloy formation). On the other hand, we did not observe any peak corresponding to ZnO which however do not disprove the presence of some amorphous or poor crystalline ZnO by the reversible conversion reaction during the charging process. Nevertheless, the alloying–dealloying based reaction for ZnO anodes is a well-acclaimed fact in the existing literature.[51,83]

Except the Zn peaks, small hump-like peaks that could be assigned to Li_2CO_3 [$(\bar{2}02)$ plane at ~30.6° (JCPDS ref. 00-022-1141)] and LiOH [(101) plane at ~32.4° (JCPDS ref. 00-032-0564)] are observed. These peaks might appear from the electrolyte as well as from hydrated Li under the environmental conditions or due to the SEI layer present at the surface of the electrode. In the case of the ZnS anode, similar metallic Zn peaks can also be observed with a relatively lower intensity. In addition, the peak observed at 54.3° for ZnO almost disappeared for the ZnS electrode at the fully charged state. Thus, it could be inferred that ZnS also undergoes the alloying–dealloying reactions between Li and Zn with a higher possibility of reversible conversion reactions as well which could lead to amorphous ZnS formation. The possibility of reversible ZnS formation is in good agreement with our dQ/dV plot (Fig. 5d) of this anode as mentioned above. In contrast to both ZnO and ZnS, the post-cycling XRD of ZnOS50 shows almost negligible peaks corresponding to any of these metallic Zn observed for the other two. This indicates that ZnOS is predominantly formed reversibly during the charging process which is eventually amorphous or very poorly crystalline in nature.[84] The established alloying–dealloying followed by reversible conversion reactions for ZnOS was also proposed in an earlier report where the electrode was grown by PLD.[51]

Thus, the superior electrochemical performance of ALD-ZnOS thin film anodes in LIBs in comparison to the pristine ZnO and ZnS anodes has been revealed. Two possible explanations can be proposed for the significantly enhanced performance of the double-ion ZnOS anode: more easily reversible reactions associated with the decomposition/reformation of ZnOS, as well as the alloying–dealloying of Li–Zn, and the higher conductivity of ZnOS. The uniform presence of O and the small amount of incorporated S facilitate the electrochemical activity against Li^+ due to improved conductivity, leading to the higher stable specific capacity of the ZnOS anode. This study explored the performance of ALD-ZnOS with a highly stable specific capacity for the first time that has been shown to be comparable to the existing literature on Zn-based anode materials in LIBs (Table S1†). In addition, with the advantages of ALD, this offers an easy and direct approach of conductive and binder additive-free electrode assembly. Further improvement in the capacity retention for ZnOS anodes could be achieved by using a 3D interconnected conducting network like multiwalled carbon nanotubes (MWCNTs), N-doped carbon cloths or porous carbon which will provide significant space for the volume change during the cycling process. Thus, it should reduce the pulverization and help improve the structural stability of the active electrode materials which could result in higher overall capacity of the electrode.[3,13,16,28,56] However, the current work should also be considered as an efficient step further towards all solid-state thin film batteries with ultrathin electrodes (<100 nm) for the future.

4. Conclusions

This work demonstrates for the first time the excellent electrochemical performance of atomic layer deposited highly polycrystalline ZnOS thin film anodes in LIBs. The optimized thickness was established for the ZnOS anodes owing to the ability to precisely control their thickness using ALD. Extremely uniform films were deposited and their respective elemental presence revealed the efficiency of the ALD process for the growth of ternary materials as active electrodes. O-rich films with significantly enhanced capacities compared to the pure ALD-ZnO anode were found due to the presence of S, which is more chemically active. On the other hand, pristine ALD-ZnS demonstrated greater capacity fading upon cycling, which is restricted to a good extent due to the fact that the ZnOS film is more conductive. Thus, we believe that ALD grown ZnOS is a better anode material for battery applications. A reasonably high reversible stable capacity of 510.3 mA h g^{-1} at a current density of 1 A g^{-1} for the optimized film thickness proves the superiority of this material beyond doubt. However, this capacity can further be enhanced by coating this material conformally on a conductive scaffold layer such as multiwall carbon nanotubes, with a greater exposed surface for deposition or by controlling the O/S ratio more precisely.

Conflicts of interest

There are no conflicts to declare.

Acknowledgements

This work was supported by the National Research Foundation of Korea (NRF) grant funded by the Korean government (MSIT-No. NRF-2018R1A2B6002268 and MOE-No. NRF-2018R1A6A1A03024334). This work was also supported by the Human Resources Development Program of the Korea Institute of Energy Technology Evaluation and Planning (KETEP) granted financial resource from the Ministry of Trade, Industry & Energy, Republic of Korea (No. 20164030201310).

Notes and references

1 M. M. Thackeray, C. Wolverton and E. D. Isaacs, *Energy Environ. Sci.*, 2012, **5**, 7854–7863.
2 M. Gu, Y. He, J. Zheng and C. Wang, *Nano Energy*, 2015, **17**, 366–383.
3 J. Li, D. Yan, X. Zhang, S. Hou, T. Lu, Y. Yao and L. Pan, *J. Mater. Chem. A*, 2017, **5**, 20428–20438.
4 Y. Li, Y. Zhao, G. Huang, B. Xu, B. Wang, R. Pan, C. Men and Y. Mei, *ACS Appl. Mater. Interfaces*, 2017, **9**, 38522–38529.
5 L. Liu, M. An, P. Yang and J. Zhang, *Sci. Rep.*, 2015, **5**, 9055.
6 X. Zhu, Y. Zhu, S. Murali, M. D. Stoller and R. S. Ruoff, *ACS Nano*, 2011, **5**, 3333–3338.
7 H. Kim, D.-H. Seo, S.-W. Kim, J. Kim and K. Kang, *Carbon*, 2011, **49**, 326–332.
8 Y. Zou and Y. Wang, *Nanoscale*, 2011, **3**, 2615–2620.
9 B. Wang, X.-L. Wu, C.-Y. Shu, Y.-G. Guo and C.-R. Wang, *J. Mater. Chem.*, 2010, **20**, 10661–10664.
10 T. Zhou, Y. Zheng, H. Gao, S. Min, S. Li, H. K. Liu and Z. Guo, *Adv. Sci.*, 2015, **2**, 1500027.

11 H. Jiang, Y. Hu, S. Guo, C. Yan, P. S. Lee and C. Li, *ACS Nano*, 2014, **8**, 6038–6046.
12 Z.-W. Fu, F. Huang, Y. Zhang, Y. Chu and Q.-Z. Qin, *J. Electrochem. Soc.*, 2003, **150**, A714–A720.
13 A. Dhara, S. K. Sarkar and S. Mitra, *Adv. Mater. Interfaces*, 2017, **4**, 1700332.
14 E. Quartarone, V. Dall'Asta, A. Resmini, C. Tealdi, I. G. Tredici, U. A. Tamburini and P. Mustarelli, *J. Power Sources*, 2016, **320**, 314–321.
15 S. Goriparti, E. Miele, F. De Angelis, E. Di Fabrizio, R. Proietti Zaccaria and C. Capiglia, *J. Power Sources*, 2014, **257**, 421–443.
16 S. Lu, H. Wang, J. Zhou, X. Wu and W. Qin, *Nanoscale*, 2017, **9**, 1184–1192.
17 Y. Feng, Y. Zhang, Y. Wei, X. Song, Y. Fu and V. S. Battaglia, *Phys. Chem. Chem. Phys.*, 2016, **18**, 30630–30642.
18 Y. S. Jang and Y. C. Kang, *Phys. Chem. Chem. Phys.*, 2013, **15**, 16437–16441.
19 X. Du, H. Zhao, Y. Lu, Z. Zhang, A. Kulka and K. Świerczek, *Electrochim. Acta*, 2017, **228**, 100–106.
20 N. Mahmood, C. Zhang and Y. Hou, *Small*, 2013, **9**, 1321–1328.
21 B. Wu, H. Song, J. Zhou and X. Chen, *Chem. Commun.*, 2011, **47**, 8653–8655.
22 H. Geng, J. Yang, Z. Dai, Y. Zhang, Y. Zheng, H. Yu, H. Wang, Z. Luo, Y. Guo, Y. Zhang, H. Fan, X. Wu, J. Zheng, Y. Yang, Q. Yan and H. Gu, *Small*, 2017, **13**, 1603490.
23 P. Zheng, Z. Dai, Y. Zhang, K. N. Dinh, Y. Zheng, H. Fan, J. Yang, R. Dangol, B. Li, Y. Zong, Q. Yan and X. Liu, *Nanoscale*, 2017, **9**, 14820–14825.
24 C. Ding, D. Su, W. Ma, Y. Zhao, D. Yan, J. Li and H. Jin, *Appl. Surf. Sci.*, 2017, **403**, 1–8.
25 D. K. Nandi, U. K. Sen, D. Choudhury, S. Mitra and S. K. Sarkar, *Electrochim. Acta*, 2014, **146**, 706–713.
26 M. B. Sreedhara, S. Gope, B. Vishal, R. Datta, A. J. Bhattacharyya and C. N. R. Rao, *J. Mater. Chem. A*, 2018, **6**, 2302–2310.
27 X. H. Huang, R. Q. Guo, J. B. Wu and P. Zhang, *Mater. Lett.*, 2014, **122**, 82–85.
28 X. Shen, D. Mu, S. Chen, B. Wu and F. Wu, *ACS Appl. Mater. Interfaces*, 2013, **5**, 3118–3125.
29 L. He, X.-Z. Liao, K. Yang, Y.-S. He, W. Wen and Z.-F. Ma, *Electrochim. Acta*, 2011, **56**, 1213–1218.
30 T. Fujieda, S. Takahashi and S. Higuchi, *J. Power Sources*, 1992, **40**, 283–289.
31 J. Wang, P. King and R. A. Huggins, *Solid State Ionics*, 1986, **20**, 185–189.
32 Y. Hwa, J. H. Sung, B. Wang, C.-M. Park and H.-J. Sohn, *J. Mater. Chem.*, 2012, **22**, 12767–12773.
33 X. Wu, S. Li, B. Wang, J. Liu and M. Yu, *RSC Adv.*, 2015, **5**, 81341–81347.
34 Y. Zhao, G. Huang, Y. Li, R. Edy, P. Gao, H. Tang, Z. Bao and Y. Mei, *J. Mater. Chem. A*, 2018, **6**, 7227–7235.
35 X. Sun, C. Zhou, M. Xie, H. Sun, T. Hu, F. Lu, S. M. Scott, S. M. George and J. Lian, *J. Mater. Chem. A*, 2014, **2**, 7319–7326.
36 Q. Xie, X. Zhang, X. Wu, H. Wu, X. Liu, G. Yue, Y. Yang and D.-L. Peng, *Electrochim. Acta*, 2014, **125**, 659–665.
37 Y. Fu, Z. Zhang, X. Yang, Y. Gan and W. Chen, *RSC Adv.*, 2015, **5**, 86941–86944.
38 L. Qiao, X. Wang, L. Qiao, X. Sun, X. Li, Y. Zheng and D. He, *Nanoscale*, 2013, **5**, 3037–3042.
39 M. Bervas, L. C. Klein and G. G. Amatucci, *J. Electrochem. Soc.*, 2006, **153**, A159–A170.
40 C. Bohnke, J. L. Fourquet, N. Randrianantoandro, T. Brousse and O. Crosnier, *J. Solid State Electrochem.*, 2001, **5**, 1–7.
41 N. Pereira, F. Badway, M. Wartelsky, S. Gunn and G. G. Amatucci, *J. Electrochem. Soc.*, 2009, **156**, A407–A416.
42 T. Minemoto, A. Okamoto and H. Takakura, *Thin Solid Films*, 2011, **519**, 7568–7571.
43 S. Sinha, D. K. Nandi, S.-H. Kim and J. Heo, *Sol. Energy Mater. Sol. Cells*, 2018, **176**, 49–68.
44 C. Platzer-Björkman, T. Törndahl, D. Abou-Ras, J. Malmström, J. Kessler and L. Stolt, *J. Appl. Phys.*, 2006, **100**, 044506.
45 R. R. Thankalekshmi and A. C. Rastogi, *J. Appl. Phys.*, 2012, **112**, 063708.
46 I. Lauermann, T. Kropp, D. Vottier, A. Ennaoui, W. Eberhardt and E. F. Aziz, *ChemPhysChem*, 2009, **10**, 532–535.
47 B. K. Meyer, A. Polity, B. Farangis, Y. He, D. Hasselkamp, T. Krämer and C. Wang, *Appl. Phys. Lett.*, 2004, **85**, 4929–4931.
48 H. L. Pan, T. Yang, B. Yao, R. Deng, R. Y. Sui, L. L. Gao and D. Z. Shen, *Appl. Surf. Sci.*, 2010, **256**, 4621–4625.
49 Y.-Z. Yoo, Z.-W. Jin, T. Chikyow, T. Fukumura, M. Kawasaki and H. Koinuma, *Appl. Phys. Lett.*, 2002, **81**, 3798–3800.
50 S. H. Deulkar, J.-L. Huang and M. Neumann-Spallart, *J. Electron. Mater.*, 2010, **39**, 589–594.
51 H. Xu, Y.-N. Zhou, F. Lu and Z.-W. Fu, *J. Electrochem. Soc.*, 2011, **158**, A285–A290.
52 B. W. Sanders and A. Kitai, *Chem. Mater.*, 1992, **4**, 1005–1011.
53 J. R. Bakke, J. T. Tanskanen, C. Hägglund, T. A. Pakkanen and S. F. Bent, *J. Vac. Sci. Technol., A*, 2012, **30**, 01A135.
54 H. K. Hong, I. Y. Kim, S. W. Shin, G. Y. Song, J. Y. Cho, M. G. Gang, J. C. Shin, J. H. Kim and J. Heo, *Sol. Energy Mater. Sol. Cells*, 2016, **155**, 43–50.
55 A. L. Dadlani, S. Acharya, O. Trejo, F. B. Prinz and J. Torgersen, *ACS Appl. Mater. Interfaces*, 2016, **8**, 14323–14327.
56 M. Yu, A. Wang, Y. Wang, C. Li and G. Shi, *Nanoscale*, 2014, **6**, 11419–11424.
57 N. P. Dasgupta, X. Meng, J. W. Elam and A. B. F. Martinson, *Acc. Chem. Res.*, 2015, **48**, 341–348.
58 S. Sinha, N. Mahuli and S. K. Sarkar, *J. Vac. Sci. Technol., A*, 2015, **33**, 01A139.
59 D. K. Nandi, S. Sahoo, S. Sinha, S. Yeo, H. Kim, R. N. Bulakhe, J. Heo, J.-J. Shim and S.-H. Kim, *ACS Appl. Mater. Interfaces*, 2017, **9**, 40252–40264.
60 X. Meng, Y. Cao, J. A. Libera and J. W. Elam, *Chem. Mater.*, 2017, **29**, 9043–9052.

61 N. Mahuli, D. Saha, S. K. Maurya, S. Sinha, N. Patra, B. Kavaipatti and S. K. Sarkar, *J. Phys. Chem. C*, 2018, **122**, 16356–16367.
62 Y. S. Jung, A. S. Cavanagh, L. A. Riley, S. H. Kang, A. C. Dillon, M. D. Groner, S. M. George and S. H. Lee, *Adv. Mater.*, 2010, **22**, 2172–2176.
63 X. Zhang, I. Belharouak, L. Li, Y. Lei, J. W. Elam, A. Nie, X. Chen, R. S. Yassar and R. L. Axelbaum, *Adv. Energy Mater.*, 2013, **3**, 1299–1307.
64 J. Zhao and Y. Wang, *Nano Energy*, 2013, **2**, 882–889.
65 J. Liu, B. Wang, Q. Sun, R. Li, T. K. Sham and X. Sun, *Adv. Mater. Interfaces*, 2016, **3**, 1600468.
66 C. Persson, C. Platzer-Björkman, J. Malmström, T. Törndahl and M. Edoff, *Phys. Rev. Lett.*, 2006, **97**, 146403.
67 G. R. Dillip, A. N. Banerjee, V. C. Anitha, B. Deva Prasad Raju, S. W. Joo and B. K. Min, *ACS Appl. Mater. Interfaces*, 2016, **8**, 5025–5039.
68 M. H. Ullah, I. Kim and C.-S. Ha, *Mater. Lett.*, 2007, **61**, 4267–4271.
69 J. Wang, Z. Wang, B. Huang, Y. Ma, Y. Liu, X. Qin, X. Zhang and Y. Dai, *ACS Appl. Mater. Interfaces*, 2012, **4**, 4024–4030.
70 T. Sarnet, T. Hatanpää, E. Puukilainen, M. Mattinen, M. Vehkamäki, K. Mizohata, M. Ritala and M. Leskelä, *J. Phys. Chem. A*, 2015, **119**, 2298–2306.
71 E. Ostreng, K. B. Gandrud, Y. Hu, O. Nilsen and H. Fjellvag, *J. Mater. Chem. A*, 2014, **2**, 15044–15051.
72 Q. Xie, Y. Ma, D. Zeng, X. Zhang, L. Wang, G. Yue and D.-L. Peng, *ACS Appl. Mater. Interfaces*, 2014, **6**, 19895–19904.
73 Q. Pan, L. Qin, J. Liu and H. Wang, *Electrochim. Acta*, 2010, **55**, 5780–5785.
74 H. Zheng, J. Li, X. Song, G. Liu and V. S. Battaglia, *Electrochim. Acta*, 2012, **71**, 258–265.
75 S. S. Zhang, *J. Power Sources*, 2006, **161**, 1385–1391.
76 S. S. Choi and H. S. Lim, *J. Power Sources*, 2002, **111**, 130–136.
77 J. Cannarella and C. B. Arnold, *J. Power Sources*, 2014, **245**, 745–751.
78 C. Peabody and C. B. Arnold, *J. Power Sources*, 2011, **196**, 8147–8153.
79 G. Garcia-Belmonte, *Electrochem. Commun.*, 2003, **5**, 236–240.
80 J. Bisquert and V. S. Vikhrenko, *Electrochim. Acta*, 2002, **47**, 3977–3988.
81 B. Wang, S. Li, J. Liu, M. Yu, B. Li and X. Wu, *Electrochim. Acta*, 2014, **146**, 679–687.
82 A.-R. Park, K.-J. Jeon and C.-M. Park, *Electrochim. Acta*, 2018, **265**, 107–114.
83 H. Köse, Ş. Karaal, A. O. Aydın and H. Akbulut, *J. Power Sources*, 2015, **295**, 235–245.
84 J. Li, D. Yan, T. Lu, Y. Yao and L. Pan, *Chem. Eng. J.*, 2017, **325**, 14–24.

